Towards the design of efficient metal free ORR catalysts based on Zeolite Templated Carbons

Thibaud Aumond, Valentin Fogiel, Leonardo Leandro dos Santos, Isabelle Batonneau-Gener, Yannick Pouilloux, Clément Comminges, Christine Canaff, Sibele B.C. Pergher, Aurélien Habrioux, Alexander Sachse

Towards the design of efficient metal free ORR catalysts based on Zeolite Templated Carbons

Thibaud Aumond,[a] Valentin Fogiel,[a] Leonardo Leandro dos Santos,[a,b] Isabelle Batonneau-Gener,[a] Yannick Pouilloux,[a] Clément Comminges,[a] Christine Canaff,[a] Sibele B. C. Pergher,[b] Aurélien Habrioux,[a*] Alexander Sachse[a*]

[a]Université de Poitiers, Institut de Chimie des Milieux et Matériaux de Poitiers (IC2MP) - UMR 7285 CNRS, UFR SFA, Bât. B27, 4 rue Michel Brunet, TSA 51106, 86073 Poitiers Cedex 9 – France.

[b]Molecular Sieves laboratory (LABPEMOL), Chemistry Institute, University of Rio Grande do Norte, Av Senador Salgado Filho, 3000, CEP : 59078-970, Natal – RN, Brazil.

*corresponding authors: aurelien.habrioux@univ-poitiers.fr,

alexander.sachse@univ-poitiers.fr

Abstract

Carbon and carbon/nitrogen Zeolite Templated Carbons (C-ZTC and CN-ZTC) were synthesized from pure ethylene and acetonitrile precursors and thoroughly characterized by nitrogen physisorption at 77 K, SEM, XRD, TGA, Raman spectroscopy and XPS. The CN-ZTC presented high nitrogen content (C/N = 12.5) and a less condensed skeleton compared to C-ZTC. Reduced micropore volume of CN-ZTC was observed due to the formation of extra-ZTC graphene-like species on the external surface, leading to high electron conductivity. The preparation of CN-ZTC based catalysts allowed for achieving conspicuously high ORR activity, featuring a half-wave potential of 0.81 V vs. RHE and high hydroxyl selectivity.

Keywords: Zeolite Templated Carbons, nitrogen functionalization, oxygen reduction reaction, graphene.

1. Introduction

Zeolite Templated Carbons (ZTCs) combine electron conductivity and high micropore volume. These unique structures have attracted much attention in recent years due to remarkable performances in a number of applications, including gas storage and energy conversion [1]. ZTCs are achieved through the polymerization of carbon precursors in the extended micropore network of a given zeolite template. After pyrolysis and dissolution of the zeolite, the ZTC is recovered and hence exhibits a negative copy of the texture of the zeolite template [2]. The exact atomistic structure of ZTCs is still a matter of debate, yet most models are based on either closed struts or open blade models [3].

Carbon-based nanomaterials are particularly interesting for their use as catalysts in electrode fuel cells, such as in the oxygen reduction reaction (ORR) [4]. The ORR occurs at the cathode of fuel cells, *e.g.* hydrogen fuel cell that converts H_2 into electricity through the H_2 oxidation reaction. In alkaline conditions, the ORR ideally proceeds through four electron transfers to transform O_2 into hydroxyl ions. This four-electron transfer is desirable for fuel cell applications, yet the less efficient two-electron pathway, which produces peroxide ion intermediates, often predominates [5].

$$O_2 + 2H_2O + 4e^- \rightleftharpoons 4OH^- \quad E° = 1.230 \text{ V vs. NHE}$$

$$O_2 + H_2O + 2e^- \rightleftharpoons HO_2^- + OH^- \quad E° = 0.695 \text{ V vs. RHE}$$

Pt-based catalysts are still the most active ORR catalysts, allowing the reaction to proceed through a four-electron path [6]. These yet present important drawbacks related to their high cost, low availability and the poor durability of Pt. Pt is indeed prone to agglomeration during electrocatalytic use and readily poisoned through CO impurities in H_2 fuel cells [7,8]. All this renders commercial Pt-based electrocatalysts in energy conversion devices improbable.

The development of metal-free catalysts represents a sound solution in the quest of circumventing the drawbacks encountered using Pt-based electrocatalysts [4]. Graphene has attracted great attention in this respect, due to its high availability. Good quality graphene can easily be obtained from graphite through oxidation and reduction treatments [9]. In order to modulate the electronic properties and to generate catalytically active sites, post-synthetic functionalization with heteroatoms (such as nitrogen or phosphor) is the most common solution [10]. This strategy yet limits the number of functional groups to a few percent. Hence, low ORR activities are generally observed for such graphene-based catalysts [11].

Ryoo and co-workers rather recently reported the use of nitrogen containing ZTCs for the use as catalysts in ORR [12,13]. They synthesized ZTCs using aqueous solutions of nitrogen-based molecules (such as acetonitrile and pyrrole), resulting in micropore materials featuring low nitrogen content (4 wt%). The approach is moreover interesting since it allows synthesizing the carbon structure and inserting nitrogen atoms in a one-step procedure. These presented high ORR activity with half-wave potentials of below 0.77 V vs. RHE in ORR using alkaline conditions. It is known that zeolites suffer from heavy dealumination in the presence of water vapor at high temperatures (>600 °C), leading to the partial or complete destruction of the zeolite framework [14]. This might negatively impact the condensation of the developing ZTCs and hence lead to higher resistive behavior.

In the present contribution, we firstly compare the ORR activity of a purely carbon-based ZTC with that of a ZTC synthesized from pure acetonitrile. The nitrogen containing ZTC-featured high nitrogen content and conductivity, and allowed to observe an important ORR activity.

2. Experimental section

2.1 Materials

Acetonitrile (Sigma Aldrich, anhydrous, 99.8%), NaX zeolite (Axence), calcium nitrate tetrahydrate (Sigma Aldrich, 99%), hydrofluoric acid (49% in water, Fisher Scientific), sodium bicarbonate (Sigma-Aldrich, 99%), boric acid (Sigma Aldrich, 99%), Hydrochloric acid (Fisher scientific, 37%) ethylene (>99.9% Air Liquide), nitrogen (99.995%, Air Liquide) and Pt-C (E-tek) were purchased and used as received.

2.2 Cation exchange of NaX zeolite

1 g of NaX was suspended in 100 mL of a 0.5 M aqueous solution of $Ca(NO_3)_2$ and stirred at 80 °C for 2 hours. The zeolite was recovered by filtration, abundantly washed with deionized water and dried at 80 °C. The exchange cycle was thereafter repeated two times. After the third exchange cycle, the zeolite was calcined at 550 °C under air for 6 hours.

2.3 Synthesis of C-ZTC

The previously prepared Ca^{2+} exchanged X zeolite was introduced in a cylindrical quartz reactor containing a frit and activated in a tubular furnace at 150 °C for 1 hour under a nitrogen flow of 150 mL min^{-1} to remove physisorbed water. The oven temperature was then raised to 790 °C and after 1 hour at this temperature, gas was switched to a mixture of 6.67 vol% ethylene in nitrogen for 4 hours. Finally, the furnace temperature was raised to 890 °C for 2 hours under nitrogen flow and then cooled down at room temperature. The hybrid compound consisting of zeolite and carbon species was recovered and treated first using concentrated HCl at 80 °C for 2 hours under stirring and then with 49 wt% HF at RT for 4 hours under stirring in order to remove the zeolite. In order to neutralize the fluoride, 60 mL

of a saturated aqueous H_3BO_3 solution was added. The mixture was then neutralized by adding 60 mL of a saturated aqueous $NaHCO_3$ solution. After 1 hour of stirring at room temperature, the carbon materials were recovered by filtration and washed using hot distilled water. After drying at 80 °C overnight, the final C-ZTC was obtained.

2.4 Synthesis of CN-ZTC

For the synthesis of CN-ZTC, the same procedure as described in 2.3 was used until the activation step at 790 °C under 150 mL min^{-1} nitrogen flow. After the activation step and still under nitrogen flow, acetonitrile was fed at 790 °C using a syringe pump with a 2.5 mL h^{-1} flow rate. After 4 hours of acetonitrile feeding, the syringe pump was stopped and the temperature was raised to 890 °C under nitrogen flow for 2 hours. Finally, the reactor was cooled to RT. The protocol used for the removal of the zeolite was the same as previously described. The final CN-ZTC was obtained after washing and drying at 80 °C.

2.5 Characterization

The structural packing density (SPD) was determined by thermogravimetric analysis (TGA) of the hybrid samples, using a SDT Q600 under synthetic air with a flow of 100 mL min^{-1}. The sample was heated up to 900 °C with a ramp of 10 °C min^{-1}. SPD corresponds to the amount of carbonaceous species (carbon and heteroatoms) per gram of zeolite ($g_C\ g_{Zeo}^{-1}$) and is calculated using equation 1.

$SPD = \frac{m_i - m_f}{m_f}$ (that corresponds to $\frac{m_c}{m_Z}$) (1)

With m_i and m_f the initial and final masses of the compound, and m_C and m_Z masses of carbonaceous species and zeolite.

Nitrogen physisorption was carried out using a Micromeritics 3Flex at 77 K. Approximately 50 mg of sample was outgassed at 350 °C for 12 h before the measurement. Microporous volumes and specific surface area were calculated through *t*-plot method. The thickness of the nitrogen layer was calculated using reference isotherms of (*i*) a non-porous silica (used for the *t*-plot of the template X zeolite) and (*ii*) graphene (used for the *t*-plot of the ZTCs) [15]. Pore size distributions were determined using non-linear density functional theory (NLDFT) models available on SAIEUS software (NLDFT model developed for carbon materials with heterogeneous structure). X-Ray powder diffraction (XRD) patterns were collected using a PANalytical Empyrean X-Ray diffractometer using CuKα radiation (1.54059 Å) from 5 to 50 °2θ ranging. Elemental analysis allowed to quantify the atomic amounts of carbon, hydrogen, nitrogen and oxygen and was performed using a Flash EA 1112/Flash 2000 Thermo. Zeolite composition was determined using ICP-OES analysis using a Perkin Elmer Optima 2000 DV apparatus. Scanning Electron Microscopy (SEM) images were obtained using a JEOL JSM-790CF microscope. Raman spectra were obtained using 514 nm excited wavelength on a Labram HR 800-UV Horiba Jobin Yvon confocal microscope equipped with a Peltier cooled CCD detector with the application of a diffraction grating with 600 lines mm^{-1} and a confocal hole of 200 µm. XPS analyses were carried out with a Kratos Axis Ultra DLD spectrometer using a monochromatic Al Kα source (1486.6 eV) operating at 180W (12mA, 15kV). The operating pressure of the spectrometer was 9 x 10^{-8} Pascal. High-resolution spectra were recorded using an analysis area of 300µm x 700 µm and 40 eV pass energy. This pass energy corresponds to Ag 3d5/2 FWHM of 0.55 eV. Data were acquired with 0.1 eV steps. The binding energy was calibrated using C1s binding energy fixed at 284.8 eV as an internal reference. The following binding energies regions were recorded: C1s, O1s, and N1s. Atomic concentration ratios were calculated using sensitivity factors provided by the manufacturer. Peak fitting was achieved with Casa XPS software (version 2.3.24) applying

Gaussian-Lorentzian profiles (Lorentzian 30%) and adding asymmetric line shape to sp^2 carbon. Electrical conductivity was measured with a solartron 12962A sample holder associated with a Solartron SI 1287 electrochemical interface and an SI 1260 impedance/gain-phase analyzer. Powder samples were crushed and introduced between two gold disk electrodes of 10 mm diameter. Distance between electrodes was measured with a micrometer and was typically comprised between 0.2 and 0.6 mm. The Ohmic resistance was measured by impedance spectroscopy at 0 V bias with 10 mV amplitude from 100 kHz to 1 Hz. The ohmic resistance value was taken for a 0° phase shift when no imaginary contribution occurs. Each conductivity value results from triplicates with a relative standard deviation ranging from 1.6 to 13%. The achieved values were normalized by the value observed for graphite.

2.6 Electrochemical measurements

Electrochemical experiments were carried out using a homemade three electrode Teflon cell at room temperature. A commercial hydrogen reference electrode (purchased by Gaskatel) and a glassy carbon slab were respectively used as reference and counter electrodes. The working electrode was a glassy carbon disk (geometric surface area of 0.196 cm^2). For each experiment, 5.8 µL of catalytic ink was deposited onto the glassy carbon disk and allowed to dry under nitrogen. The catalytic ink was performed by mixing 10 mg of catalytic powder, 750 µL of ultra-pure water, 250 µL of isopropanol and 60 µL of Nafion solution (5wt.% in a solution of aliphatic alcohols). The dispersion was finally dispersed by sonication to obtain a homogeneous solution. All experiments were carried out using a rotating disk electrode (Methrohm). All electrodes were connected to a biologic SP-300 potentiostat. The electrolyte was a 0.1 mol L^{-1} KOH solution saturated with nitrogen or dioxygen. Linear sweep voltammograms were recorded at different rotating rates (400 rpm, 600 rpm, 900 rpm, 1600 rpm) by applying a scan rate of 5 mV s^{-1} to be under steady-state conditions.

3. Results and Discussion

The zeolite X template presents a Si/Al ratio of 1.13 and a Ca/Al ratio of 0.49. The zeolite features a microporous material characteristic type I nitrogen physisorption isotherm and a micropore volume of 0.31 cm^3 g^{-1} (**Figure 1**). The zeolite presents characteristic XRD peaks of the FAU phase and typical bipyramidal morphology.

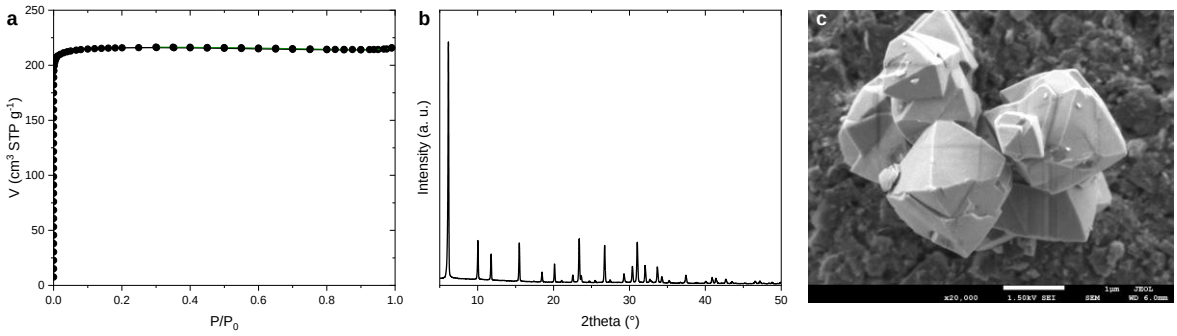

Figure 1. Nitrogen physisorption isotherm at 77 K (a), XRD powder pattern (b) and SEM image of the zeolite X template.

Two different precursors were used for the synthesis of ZTCs, *i.e.* ethylene and acetonitrile, leading to C-ZTC and CN-ZTC respectively (**Scheme 1**).

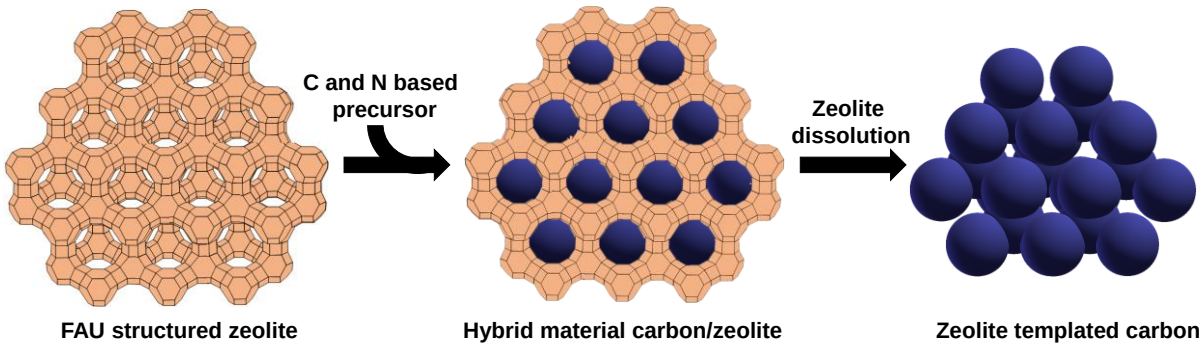

Scheme 1. Synthesis of Zeolite Templated Carbons (artist's rendition).

Both precursors allow to completely obstruct the microporosity of the zeolite template. From the weight loss at TGA of the hybrid materials, the structural packing density (SPD) was calculated, which amounts to 0.30 and 0.34 $g_C\ g_Z^{-1}$ for C-hybrid and CN-hybrid, respectively (**Figure 2a**). The slightly higher value for the CN-hybrid might indicate that some carbonaceous materials were formed on the surface of the zeolite crystals. It is further important to note that the weight loss is shifted to higher temperatures for the CN-hybrid (maximum heat flow raised for temperatures of 485 and 554 °C for C- and CN-hybrid respectively) which might be due to the presence of the nitrogen and to a different degree of condensation in the carbon skeleton. The heat of combustion for C- and CN-hybrid was calculated to be 5.7 and 11.7 kJ g^{-1}, respectively, which further indicates the different chemical nature of the samples.

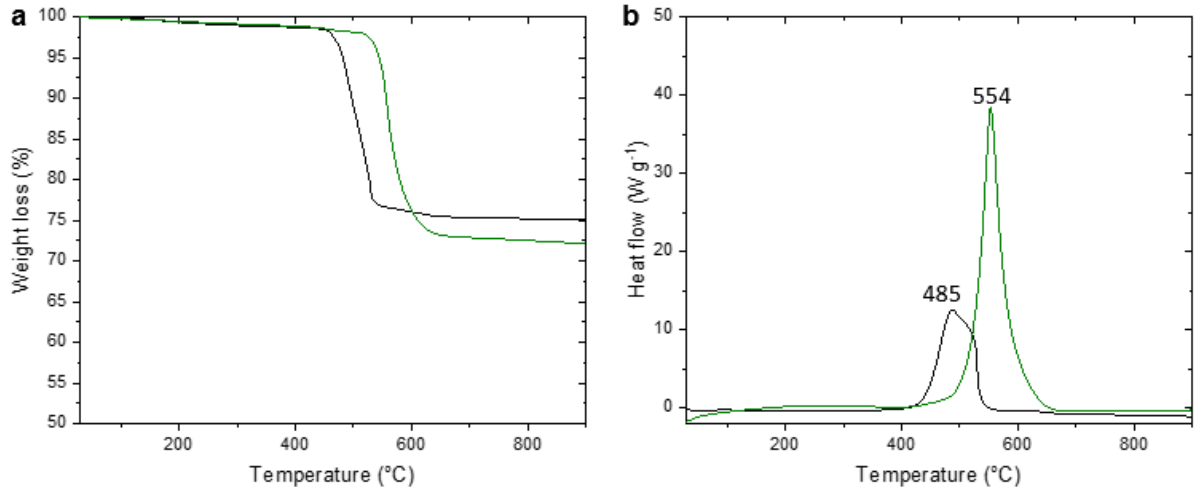

Figure 2. TGA weigh loss curves (a) and heat flow as a function of the temperature (b) of the C-hybrid (black) and CN-hybrid (green).

After dissolution of the zeolite the C-ZTC and CN-ZTCs were achieved. From the SEM images, very similar morphological features compared to the template zeolite were observed,

which indicates that for both sample particles with similar shapes and size were achieved (**Figure 3**).

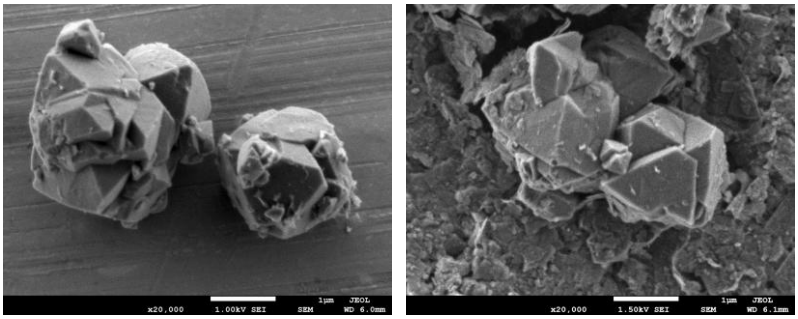

Figure 3. SEM images of C-ZTC (left) and CN-ZTC (right). Scale-bare: 1µm.

The choice of the precursor molecule importantly impacts the textural properties of the final ZTC. Both materials, C-ZTC and CN-ZTC, present type I nitrogen physisorption isotherms (**Figure 4a**). Yet, the C-ZTC features a micropore volume of 1.101 cm^3 g^{-1}, which is approximately twice as high as the volume calculated for CN-ZTC (**Table 1**). The desorption branch achieves similar nitrogen volume values as for the adsorption at a relative pressure of 0.43, which indicates that the skeleton is highly cross-linked in both cases [16]. A similar NLDFT pore size distribution was observed for both samples, indicating that the templating ability is similar for ethylene and acetonitrile in the applied conditions (**Figure 4b**). The C-ZTC presents a peak in the XRD powder pattern centered at 6.4 °2θ, which is due to structural long-range order of the carbon skeleton (**Figure 4c**). As far as the CN-ZTC is concerned, a larger peak is here observed, which suggests higher structural irregularity in the skeleton. Moreover, a larger peak in the XRD powder pattern of CN-ZTC at around 24 °2θ was observed, which can be ascribed to the (002) reflection resulting from the stacking of

graphene-like subunits [17]. The formation of such graphene layers on the surface of the ZTC particles probably explains the reduced micropore volume observed for the CN-ZTC. A further indication of the formation of such extra-ZTC species was indicated by the higher SPD for the CN-ZTC compared to the C-ZTC. Here from, it is possible to estimate that approximately 10% of the carbon/nitrogen develops on the external surface for CN-ZTC. This is most probably also the reason for the higher electron conductivity of CN-ZTC compared to the C-ZTC (**Table 2**). From TGA, full combustion of both samples can be observed at 660 °C and from which the absence of any zeolite residue can be inferred (**Figure 4d**). It is further interesting to note that the CN-ZTC presents a higher degree of water (weight loss below 100 °C), which is probably due to the higher hydrophilicity of the material due to the presence of nitrogen.

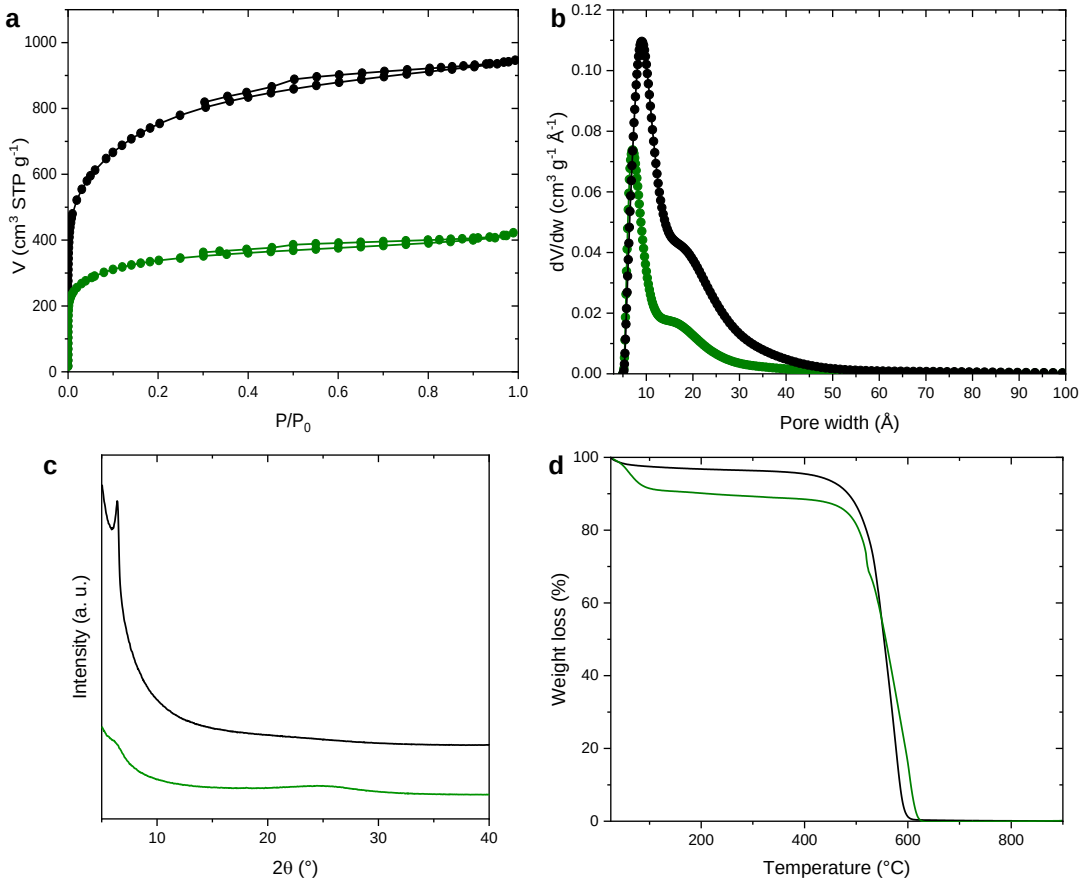

Figure 4. Nitrogen physisorption isotherms at 77 K (a), NLDFT pore size distribution (b), XRD powder patterns (c) and TGA weight loss curves (d) of C-ZTC (black) and CN-ZTC (green).

Table 1. Chemical and textural properties of C-ZTC and CN-ZTC.

	SPD ($g_C\ g_Z^{-1}$)	V_{micro} ($cm^3\ g^{-1}$)	S_{BET} ($m^2\ g^{-1}$)	C/H	C/N	Normalized conductivity ($S\ m^{-1}$)*
C-ZTC	0.30	1.01	2748	7.4	-	0.05
CN-ZTC	0.34	0.48	1230	3.5	12.9	0.35

*Normalized by the value recorded for graphite.

Major differences in the chemical nature of the samples were deduced through elemental analysis. Whilst the C-ZTC features a C/H ratio of 7.4, this ratio is significantly lower for CN-ZTC and amounts to 3.5. This clearly indicates that the skeleton in C-ZTC contains a higher degree of condensed aromatic cycles compared to CN-ZTC. To further investigate the chemical nature of the samples Raman spectra were recorded, which present typical features for carbon-based materials, such as for graphene and activated carbons [18,19]. The decomposition of the spectra allowed to distinguish six contributions [20]. The G band, which is ascribed to the bond stretching of all pairs of sp^2 carbon atoms, is centered at 1597 and 1604 cm^{-1} for C-ZTC and CN-ZTC, respectively. The blue-shift of the G-mode for the CN-ZTC can be ascribed to the presence of extra-ZTC graphene-like carbon [21]. The D band, resulting from the breathing mode of sp^2 carbon atoms in cycles, is centered at 1328 and 1348 cm^{-1} for C-ZTC and CN-ZTC, which allows for a similar conclusion as for the G mode. The

relation of the intensities of the D and G mode is a mean to assess the amount of defects or edges in graphene-based materials. The I_D/I_G ratio is higher for the CN-ZTC (1.3 vs. 1.1 for C-ZTC), indicating a reduced skeleton thickness. Indeed L_a, *i.e.* the lateral distance [20], amounts to 4.11 and 3.49 nm for C-ZTC and CN-ZTC, respectively, confirming well the less condensed skeleton as inferred from the C/H ratio of materials. The higher intensity of the G-mode of the CN-ZTC can be ascribed to the formation of pyrrolic N, which might feature sp^3 carbons [22]. Indeed, the presence of sp^3 carbons can be further deduced from the higher contribution, classically ascribed as amorphous band [23], centered at 1566 cm^{-1} in CN-ZTC.

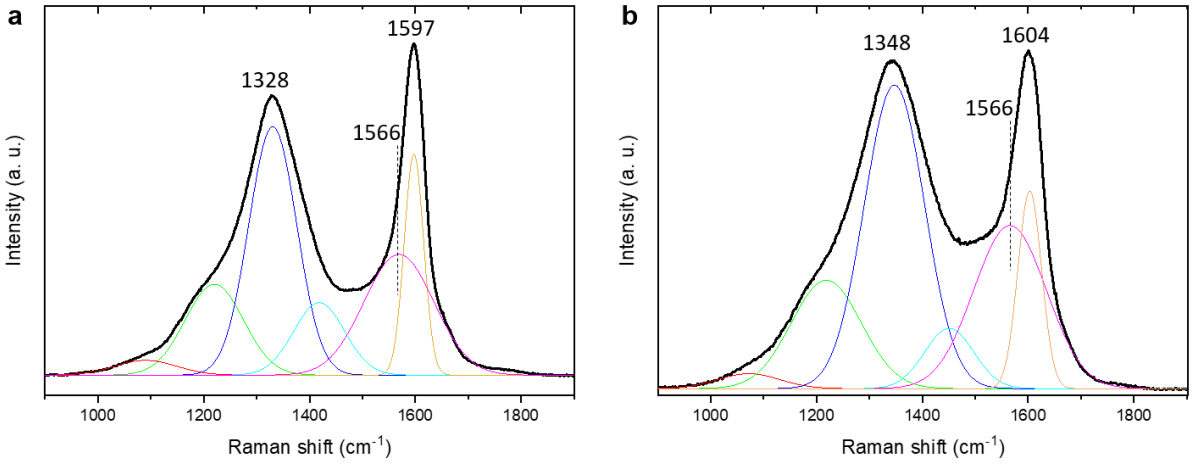

Figure 5. Raman spectra and decomposition of C-ZTC (a) and CN-ZTC (b).

This is further confirmed by the XPS spectra (**Figure 6**). Important differences can be drawn from the observation of the C1s photoelectron peak, which is larger for CN-ZTC and features a full width at half maximum (FWHM) of 1.8 eV, compared to 0.9 eV for the C-ZTC. It can generally be concluded that the larger the FWHM the more defects in the carbon structures (higher degree of carbon speciations) [24], which confirms the observation of the higher I_D/I_G ratio for the CN-ZTC calculated from Raman spectra. The C1s peak for C-ZTC and CN-ZTC is centered at 284.5 and 284.9 eV, respectively. It is to recall that pure graphene presents a

C1s peak typically centered at 284.4 eV (aromatic sp^2 carbon) [25]. With increasing sp^3 character the peak shifts to higher energies, typically observed for graphene with structural defects [26]. This observation hence suggests that the CN-ZTC features a higher degree of sp^3 carbon, which is in agreement with the lower C/H ratio measured for this sample.

A C/N ratio of 12.8 was measured by elemental analysis and confirmed by XPS. The N1s photoelectron peak observed for CN-ZTC could be decomposed into five contributions. Predominant contributions centered at 398.3, 399.3 and 401.0 eV were observed, which can be ascribed to the presence of pyridinic, pyrrolic and graphitic nitrogen, which amount to 24.2%, 8.5% and 49.4% of the total nitrogen species, respectively. The contributions at higher binding energy are due to pyridinic-oxide and π- π^* N sp^2 interactions. Indeed, higher oxygen content was measured for the CN-ZTC and amounts to C/O ratio of 8.2, whilst the C/O ratio of the C-ZTC was found to be 20.0.

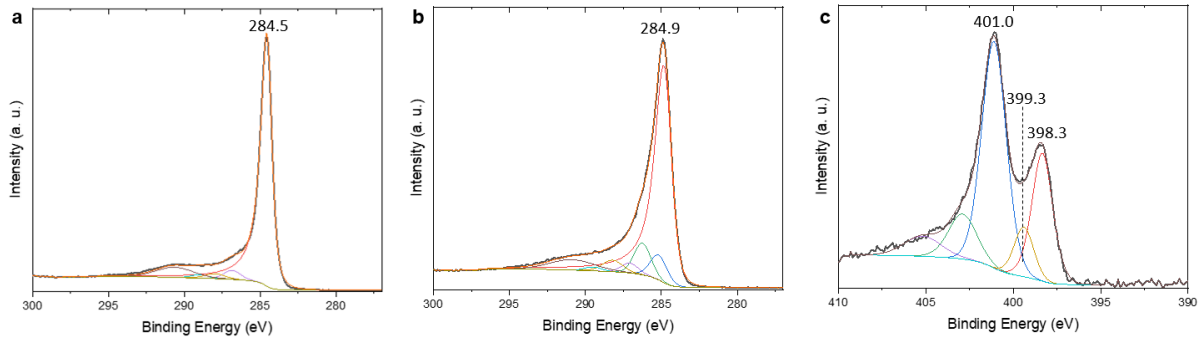

Figure 6. X-ray C1s photoelectron peak of C-ZTC (a) and CN-ZTC (b). X-ray N1s photoelectron peak of CN-ZTC (c).

The ORR activity of C-ZTC and CN-ZTC was evaluated by recording polarization curves at different rotating rates in the 1.0 – 0.2 potential range (**Figure S1**). A comparison of polarization curves recorded at 1600 rpm using C-ZTC, CN-ZTC and a reference Pt/C

catalyst is presented in **Figure 7a**. For C-ZTC and CN-NZTC samples, in reason of the large capacitive current, polarization curves were corrected by subtracting the current obtained in a nitrogen saturated electrolyte. Both C-ZTC and CN-ZTC catalysts feature high ORR activity that can be associated with their large specific surface areas (**Table 1**). CN-ZTC catalysts yet allowed for observing higher activities, achieving a half-wave potential of 0.81 V vs. RHE; a value which is slightly below that of the noble metal-containing Pt/C catalyst (0.86 V vs. RHE). These performances are slightly higher than that of classical N-doped graphene obtained from doping of graphene oxide [27] and are very similar to those obtained with recently developed biomass derived N-doped carbons [28].

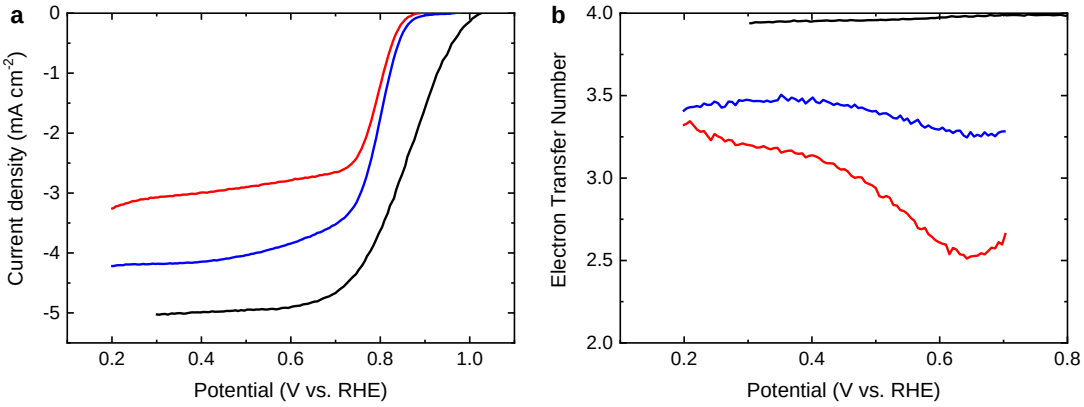

Figure 7. a) Polarization curves recorded with C-ZTC (red), CN-ZTC (blue) and a reference Pt-C catalyst (black) in an oxygen saturated 0.1 mol L^{-1} KOH electrolyte at a rotation rate of 1600 rpm and at a scan rate of 5 mV s^{-1}. b) Number of electrons exchanged per oxygen molecule as a function of the applied electrode potential for C-ZTC (red), CN-ZTC (blue) and Pt-C catalysts (black).

The higher ORR activity of CN-ZTC in comparison to C-ZTC is clearly associated to the high percentage of nitrogen atoms as well as a higher electronic conductivity facilitating charge

transfer. Since CN-ZTC and C-ZTC exhibit the same morphostructural properties, this allows assessing that nitrogen functionalization and conductivity are important factors determining ORR activity more than specific surface area and structural long-range order. It is interesting to note that most of the nitrogen atoms in the CN-ZTC are of pyridinic or graphitic-like speciation. These latter are known to be the most efficient active sites for ORR [29]. Guo *et al.* demonstrated that the pyridinic nitrogen atoms were responsible for the formation of Lewis base sites on the adjacent carbon, which favor oxygen adsorption and facilitate the reduction process [30]. Moreover, it has been speculated that graphitic nitrogen decreases electron density on adjacent carbon atoms [29], thus promoting ORR.

Based on the polarization curves recorded at different rotation rates, Koutecky-Levich plots presenting the evolution of j^{-1} as a function of $\Omega^{-1/2}$ were obtained (**Figure S2**). The slope of linear fits was used to determine the number of electrons exchanged per oxygen molecule (*n*) during the reduction process, according to the Koutecky-Levich equation [31]:

$$\frac{1}{j} = \frac{1}{j_L} + \frac{1}{j_k} = \frac{1}{B\sqrt{\Omega}} + \frac{1}{j_k}$$

With $B = 0.2nFC_{O_2}D_{O_2}^{\frac{2}{3}}\nu^{-\frac{1}{6}}$

In these equations, j, j_k and j_L are respectively the total current density, the kinetic current density and the diffusion limited current density. Ω (rpm) represents the angular velocity, F is the Faraday constant (96485 C mol^{-1}), C_{O_2} is the bulk oxygen concentration (1.2 10^{-6} mol cm^{-3} in 0.1 mol L^{-1} KOH electrolyte) [32], ν is the kinematic viscosity of the electrolyte (0.01 cm^2 s^{-1}) [30] and D_{O_2} is the diffusion coefficient of molecular oxygen in a 0.1 mol L^{-1} KOH electrolyte (1.90 10^{-5} cm^2 s^{-1}) [33]. The constant 0.2 is used when Ω is expressed in rotation per minute. The evolution of *n* as a function of the applied electrode potential is presented in **Figure 7b** for C-ZTC, CN-NZTC as well as for a commercial Pt/C (10 wt.%) catalyst. For C-

ZTC the electron transfer number drifts from 3.5 to 2.5 with increasing potential, indicating that both the two-electron and four-electron pathways are involved during the reduction reaction. By revenge an almost constant value of 3.5 is achieved for CN-ZTC, which indicates that the catalyst promotes rather the four-electron route, allowing hence for superior hydroxyl selectivity.

4. Conclusion

High nitrogen content in ZTCs could be achieved by the use of pure acetonitrile as precursor. The CN-ZTC featured morphological and textural characteristics similar to C-ZTC synthesized using ethylene. Reduced textural properties of the NC-ZTC could be ascribed to the presence of some extra-ZTC graphene-like species formed on the external surface. Significant differences in the composition of the CN-ZTC were observed in comparison to C-ZTC, such as lower skeleton condensation and higher conductivity. Superior ORR activity was observed for the nitrogen containing ZTC achieving high half-wave potential and hydroxyl selectivity. The achieved results indicate that adjusting synthetic conditions could allow for tuning nitrogen content in ZTCs and hence their electronic properties, which would pave the way for the development of metal-free catalysts with excellent ORR activity.

Supporting Information

Polarization curves and Koutecky-Levich plots are available as supporting information.

ACKNOWLEDGMENTS

The authors acknowledge financial support from the European Union (ERDF) and "Région Nouvelle Aquitaine" and the CAPES-COFECUB program with the reference 45020TE.

References

[1] H. Nishihara, T. Kyotani, Zeolite-templated carbons – three-dimensional microporous graphene frameworks, Chem. Commun. 54 (2018) 5648-5673. https://doi.org/10.1039/C8CC01932K.

[2] T. Aumond, M. Esteves, Y. Pouilloux, R. Faccio, A. Sachse, Impact of the crystal size of beta zeolite on the structural quality of zeolite templated carbons, Microporous Mesoporous Mater. 331 (2022) 111644. https://doi.org/10.1016/j.micromeso.2021.111644.

[3] E.E. Taylor, K. Garman, N.P. Stadie, Atomistic Structures of Zeolite-Templated Carbon, Chem. Mater. 32 (2020) 2742–2752. https://doi.org/10.1021/acs.chemmater.0c00535.

[4] L. Dai, Y. Xue, L. Qu, H.-J. Choi, J.-B. Baek, Metal-Free Catalysts for Oxygen Reduction Reaction, Chem. Rev. 115 (2015) 4823–4892. https://doi.org/10.1021/cr5003563.

[5] M. Winter, R.J. Brodd, What Are Batteries, Fuel Cells, and Supercapacitors?, Chem. Rev. 104 (2004) 4245-4270. https://doi.org/10.1021/cr020730k.

[6] S. Mukejee, S. Srinivasan, M.P. Soriaga, J. Mcbreen, Role of Structural and Electronic Properties of Pt and Pt Alloys on Electrocatalysis of Oxygen Reduction: An In Situ XANES and EXAFS Investigation J. Electrochem. Soc. 142 (1995) 1409. https://doi.org/10.1149/1.2048590.

[7] K. Kinoshita, Particle Size Effects for Oxygen Reduction on Highly Dispersed Platinum in Acid Electrolytes, J. Electrochem. Soc. 137 (1990) 845. https://doi.org/10.1149/1.2086566.

[8] B. C. H. Steele, A. Heinzel, Materials for fuel-cell technologies, Nature, 414 (2001) 345–352. https://doi.org/10.1038/35104620.

[9] D.P. Hansora, N.G. Shimpi, S. Mishra, Graphite to Graphene via Graphene Oxide: An Overview on Synthesis, Properties, and Applications, *JOM* 67 (2015) 2855–2868. https://doi.org/10.1007/s11837-015-1522-5.

[10] C. Hu, D. Liu, Y. Xiao, L. Dai, Functionalization of graphene materials by heteroatom-doping for energy conversion and storage, Prog. Nat. Sci.: Mater. Int. 28 (2018) 121-132. https://doi.org/10.1016/j.pnsc.2018.02.001.

[11] X. Tong, X. Zhan, D. Rawach, Z. Chen, G. Zhang, S. Sun, Low-dimensional catalysts for oxygen reduction reaction, Prog. Nat. Sci.: Mater. Int. 30 (2020) 787-795. https://doi.org/10.1016/j.pnsc.2020.09.011.

[12] Y. Kwon, K. Kim, R. Ryoo, N-doped zeolite-templated carbon as a metal-free electrocatalyst for oxygen reduction, *RSC Adv.* 6 (2016) 43091-43097. https://doi.org/10.1039/C6RA08085E.

[13] S.W. Han, J. Bang, S.H. Ko, R. Ryoo, Variation of nitrogen species in zeolite-templated carbon by low-temperature carbonization of pyrrole and the effect on oxygen reduction activity, J. Mater. Chem. A 7 (2019) 8353-8360. https://doi.org/10.1039/C9TA01621J.

[14] J.A. Rabo, M.W. Schoonover, Early discoveries in zeolite chemistry and catalysis at Union Carbide, and follow-up in industrial catalysis, Appl. Catal. A 222 (2001) 261-275. https://doi.org/10.1016/S0926-860X(01)00840-7.

[15] T. Aumond, J. Rousseau, Y. Pouilloux, L. Pinard, A. Sachse, Synthesis of hierarchical zeolite templated carbons, Carbon Trends 2 (2021) 100014. https://doi.org/10.1016/j.cartre.2020.100014.

[16] J. Weber, J. Schmidt, A. Thomas, W. Böhlmann, Micropore Analysis of Polymer Networks by Gas Sorption and 129Xe NMR Spectroscopy: Toward a Better

Understanding of Intrinsic Microporosity, Langmuir 26 (2010) 15650–15656. https://doi.org/10.1021/la1028806.

[17] B. Qi, L. Di, W. Xu, X. Zhang, Dry plasma reduction to prepare a high performance Pd/C catalyst at atmospheric pressure for CO oxidation, J. Mater. Chem. A 2 (2014) 11885-11890. https://doi.org/10.1039/C4TA02155J.

[18] A.C. Ferrari, J. Robertson, Raman spectroscopy of amorphous, nanostructured, diamond–like carbon, and nanodiamond, Philos. Trans. R. Soc. 362 (2004) 2477-2512. https://doi.org/10.1098/rsta.2004.1452.

[19] A. Lazzarini, A. Piovano, R. Pellegrini, G. Leofanti, G. Agostini, S. Rudić, M. R. Chierotti, R. Gobetto, A. Battiato, G. Spoto, A. Zecchina, C. Lamberti, E. Groppo, A comprehensive approach to investigate the structural and surface properties of activated carbons and related Pd-based catalysts, Catal. Sci. Technol. 6 (2016) 4910-4922. https://doi.org/10.1039/C6CY00159A.

[20] A.C. Ferrari, J. Robertson, Interpretation of Raman spectra of disordered and amorphous carbon, Phys. Rev. B 61 (2000) 14095-14107. https://doi.org/10.1103/PhysRevB.61.14095.

[21] Q.-H. Yang, P.-X. Hou, M. Unno, S. Yamauchi, R. Saito, T. Kyotani, Dual Raman Features of Double Coaxial Carbon Nanotubes with N-Doped and B-Doped Multiwalls, Nano Lett. 5 (2005) 2465-2469. https://doi.org/10.1021/nl051779j.

[22] J. Li, X. Li, P. Zhao, D.Y. Lei, W. Li, J. Bai, Z. Ren, X. Xu, Searching for magnetism in pyrrolic N-doped graphene synthesized via hydrothermal reaction, Carbon, 84 (2015) 460-468, https://doi.org/10.1016/j.carbon.2014.12.024.

[23] M.W. Smith, I. Dallmeyer, T.J. Johnson, C.S. Brauer, J.-S. McEwen, J.F. Esoinal, M. Garcia-Perez, Structural analysis of char by Raman spectroscopy: Improving band

assignments through computational calculations from first principles, Carbon 100 (2016) 678-692. https://doi.org/10.1016/j.carbon.2016.01.031.

[24] J. Lahaye, G. Nanse, P. Fioux, A. Bagreev, A. Broshnik, V. Strelko, Chemical transformation during the carbonisation in air and the pyrolysis under argon of a vinylpyridine divinylbenzene copolymer by X-ray photoelectron spectroscopy, Appl. Surf. Sci. 147 (1999) 153-174. https://doi.org/10.1016/S0169-4332(99)00108-7.

[25] T. Susi, T. Pichler, P. Ayala , X-ray photoelectron spectroscopy of graphitic carbon nanomaterials doped with heteroatoms, Beilstein J. Nanotechnol. 6 (2015) 177–192. https://doi.org/10.3762/bjnano.6.17.

[26] D.J. Morgan, Comments on the XPS Analysis of Carbon Materials, J. Carbon Res. 7 (2021) 51–59. https://doi.org/10.3390/c7030051.

[27] L.M. Rivera, G. García, E. Pastor, Novel graphene materials for the oxygen reduction reaction, Curr. Opin. Electrochem., 2018, 9, 233-239. https://doi.org/10.1016/j.coelec.2018.05.009

[28] S. Park, J. Kim, K. Kwon, A review on biomass-derived N-doped carbons as electrocatalysts in electrochemical energy applications, Chem. Eng. J., 2022, 446, 137116. https://doi.org/10.1016/j.cej.2022.137116

[29] J. Quílez-Bermejo, M. Melle-Franco, E. San-Fabián, E. Morallón, D. Cazorla-Amorós, Towards understanding the active sites for the ORR in N-doped carbon materials through fine-tuning of nitrogen functionalities: an experimental and computational approach, J. Mater. Chem. A 7 (2019) 24239-24250. https://doi.org/10.1039/C9TA07932G.

[30] D. Guo, R. Shibuya, C. Akiba, S. Saji, T. Kondo and J. Nakamura, Active sites of nitrogen-doped carbon materials for oxygen reduction reaction clarified using model catalysts, Science, 2016, 351, 361–365. DOI: 10.1126/science.aad0832.

[31] E. Gileadi, Electrodes Kinetics for Chemists, Chemical Engineers, and Materials Scientists; Wiley-VCH: New York, N Y, USA, 1993, p 616.

[32] K.E. Gubbins, R.D. Walker, The Solubility and Diffusivity of Oxygen in Electrolytic Solutions. *J. Electrochem. Soc.* **1965**, *112*, 469– 471. https://doi.org/10.1149/1.2423575.

[33] H. Zhao, L. Li, Y. Liu, X. Geng, H. Yang, C. Sun, B. An, Synthesis and ORR performance of nitrogen-doped ordered microporous carbon by CVD of acetonitrile vapor using silanized zeolite as template, Appl. Surf. Sci. 504 (2020) 144438. https://doi.org/10.1016/j.apsusc.2019.144438.